Biosensors and Bioelectronics 214 (2022) 114493

Contents lists available at ScienceDirect

Biosensors and Bioelectronics

journal homepage: www.elsevier.com/locate/bios

Terahertz meta-biosensor based on high-Q electrical resonance enhanced by the interference of toroidal dipole

Chiben Zhang[a,b], Tingjia Xue[c], Jin Zhang[a], Zhenfei Li[a], Longhai Liu[d,e], Jianhua Xie[d], Jianquan Yao[e], Guangming Wang[b,***], Xiaodan Ye[c,f,**], Weiren Zhu[a,*]

[a] Department of Electronic Engineering, Shanghai Jiao Tong University, Shanghai, 200240, China
[b] Air and Missile Defense College, Air Force Engineering University, 710051, Xi'an, China
[c] Department of Radiology, Shanghai Chest Hospital, Shanghai Jiao Tong University, Shanghai, 200030, China
[d] Advantest (China) Co., Ltd. Shanghai, 201203, China
[e] College of Precision Instruments and Opto-Electronics Engineering, Institute of Laser and Optoelectronics, Tianjin University, Tianjin, 300072, China
[f] Department of Radiology, Shanghai Institute of Medical Imaging, Zhongshan Hospital, Fudan University, 180 Fenglin Road, Shanghai, 200032, China

ARTICLE INFO

Keywords:
Biosensing
Metasurfaces
Interference enhancement
Lung cancer detection
Terahertz

ABSTRACT

Electrical dipole resonances typically have low *Q* factor and broad resonant linewidth caused by strong free-space coupling with high radiative loss. Here, we present a strategy for enhancing the *Q* factor of the electrical resonance via the interference of a toroidal dipole. To validate such a strategy, a metasurface consisting of two resonators is designed that responsible to the electric and toroidal dipoles. According to constructive and destructive hybridizations of the two dipole modes, enhanced and decreased *Q* factors are found respectively for the two hybrid modes, compared to the one for the conventional electric dipole resonance. As a practical application of such high *Q* resonance, we further experimentally investigate the sensing performance of the metasurface biosensor by detecting the cell concentration of lung cancer cells (type A549). Moreover, through monitoring both resonance frequency and amplitude variation of the metasurface biosensor, the dielectric permittivity of the lung cancer cells is delicately estimated by the conjoint analysis of both simulated and measured results. Our proposed metasurface paves a promising way for the study of multipole interference in the field of nanophotonics and validates its effectiveness in biomedical sensing.

1. Introduction

The study of multipolar interference, which related in interference between electric and magnetic dipole modes for a hypothetical magnetic sphere was proposed by Kerker in 1983Kerker et al. (1983). Due to the sophisticated construction of independent multipoles and the lack of experimental support, it has not attracted widespread attention. Until recently, with the development of artificial metamaterials and their convenience in fabrication, a variety of dipoles or modes can be systematically constructed by subwavelength resonators, and thus the Kerker effect has promoted and rapidly permeated various branches of modern nanophotonics Liu and Kivshar (2018). As a result, numerous interesting light-matter interactions or mechanisms have been proposed. For example, the constructive or destructive interference by electric and magnetic dipolar resonances could lead to remarkable scattering properties of subwavelength artificial dielectric particles in the forward or backward directions Kerker et al. (1983); Liu and Kivshar (2018); Shamkhi et al. (2019). Besides, the two dipoles can be commonly constructed as bright and dark modes with disparate quality (*Q*) factor to analogue the electromagnetically induced transparency (EIT) Tassin et al. (2009); Yang et al. (2014); Yin et al. (2013); Zhang et al. (2010), which could motivate an extremely narrow reflection or transmission window. Furthermore, the higher order multipoles González-Alcalde et al. (2019), Fano Tan et al. (2020), and lattice Lou et al. (2021) modes could also be easily configured by metasurfaces Zhang et al. (2020); Li et al. (2018); Zhang et al. (2021a); Li et al. (2022), a kind of two-dimensional counterparts of metamaterials, to construct hybridized interference resonances.

* Corresponding author.
** Corresponding author. Department of radiology, Shanghai Chest Hospital, Shanghai Jiao Tong University, Shanghai, 200030, China.
*** Corresponding author.
E-mail addresses: wgming01@sina.com (G. Wang), yuanyxd@163.com (X. Ye), weiren.zhu@sjtu.edu.cn (W. Zhu).

https://doi.org/10.1016/j.bios.2022.114493
Received 19 March 2022; Received in revised form 15 June 2022; Accepted 17 June 2022
Available online 27 June 2022
0956-5663/© 2022 Elsevier B.V. All rights reserved.

Distinct from the magnetic and electric dipoles, the toroidal dipole is predicted by Zel'dovich owing to its exotic localized electromagnetic excitation and non-standard multipoles configuration Zel'Dovich (1958). It can exist in various scales including nuclear Flambaum and Murray (1997), atomic Flambaum and Khriplovich (1980), and molecular Lemak et al. (2013). The electric dipole is generated by a pair of opposite charges with oscillating charge density and the magnetic dipole to be created by a current loop and the toroidal dipole can be regarded as currents flowing on the surface of the torus along its meridians Papasimakis et al. (2016); Yang et al. (2021); Kaelberer et al. (2010). After almost a decade, the toroidal moments were excluded from the family of electric and magnetic moments in electrodynamics by the multipolar expansion Dubovik and Tugushev (1990); Talebi et al. (2018). The establishment of toroidal moments in a spatially confined interference leads to singular properties of weak free-space coupling, circular dichroism, and enhanced light-matter interaction, which open up possibilities for new magnetoelectric phenomena as well as potential applications in data storage Naumov et al. (2009), polarization twister Guo et al. (2014), and lasing spacer Huang et al. (2013). Further attempts have been devoted on the study of resonance interference by hybridizing different type of dipoles or modes in the platform of metasurfaces to explore unusual phenomena such as anapole transmission Wu et al. (2018), dual-sensitive detecting Lou et al. (2021), and polarization-independent Fano resonance Wang et al. (2020). The interference-based resonances show sharper line shape compared to those in conventional resonances induced by single dipole, making them extremely suitable for sensing applications, for example, highly sensitive and label-free biosensors for cells Zhang et al. (2021b); Yang et al. (2019); Zhang et al. (2022); Yan et al. (2019) and proteins Alici (2014); Cheng et al. (2020); Yan et al. (2022) detecting.

In this work, we propose a sensitive biosensor based on multipolar interference in a metasurface with high-Q electrical resonance, which could detect the concentration and permittivity of lung cancer cells by analyzing two-dimensional THz spectra. The high-Q electrical resonance (mode I) is generated owing to the enhancement of the electric dipole by the toroidal dipole, as well as another low-Q mode (mode II) is formed by the cancellation of the two dipoles. The Q factor reach 45.9 as maximum on mode I, which is far more than the electric dipole resonance (~ 10) that generates only by single cut wire. Further, the refractive index sensitivity of the biosensor is as high as 403.7 GHz/RIU (Refractive Index Unit). For practical, we attain a regular variation in both amplitude and frequency with concentration of lung cancer cells (A549) cultured on the biosensors, which have a good agreement with the simulation. Therefore, the precise cell concentration can be quickly determined by the novel biosensor based on its linear relationship with respective to the frequency shift as observed. Furthermore, both the refraction index and permittivity of the A549 lung cancer cell are calculated by combining simulation and experimental results. The proposed novel strategy not only enhance the Q factor of sensors but also has the potential for realizing free-label, precise and comprehensive detection for lung cancer cells.

2. Biosensor design and theory

2.1. Metasurface design

Fig. 1(a) shows the metasurface biosensor covered with lung cancer cells under the illumination of THz waves, where the shift of the transmission spectrum could give an index to the slight variation of the analytes. The unit cell of the metasurface biosensor consists of a pair of mirrored gold spit ring resonators (SRRs) and a cut wire sandwiched between them, which were covered on a 500 μm-thick quartz glass substrate ($\epsilon_q = 3.85$) with the size of 5×5 mm^2. All gold patterns are fabricated by projection step photolithography followed by the deposition of 10 nm Ti and 150 nm Au layers with DC conductivity of 4.56×10^7 S/m by magnetron sputtering. The A549 lung cancer cells with different concentrations are cultured on the metasurface as displayed in Fig. 1(b) and the detailed method of cell culturalization are shown in the experimental section.

For a typical electric dipole resonator, i.e., a metallic cut wire, as shown in the top of Fig. 1(c), current flows from a negative charge at one end to a positive charge at the other end, which generates a magnetic field (m, red arrow) around it. For another part, the toroidal dipole could be excited head-to-tail magnetic field, which produced by the currents

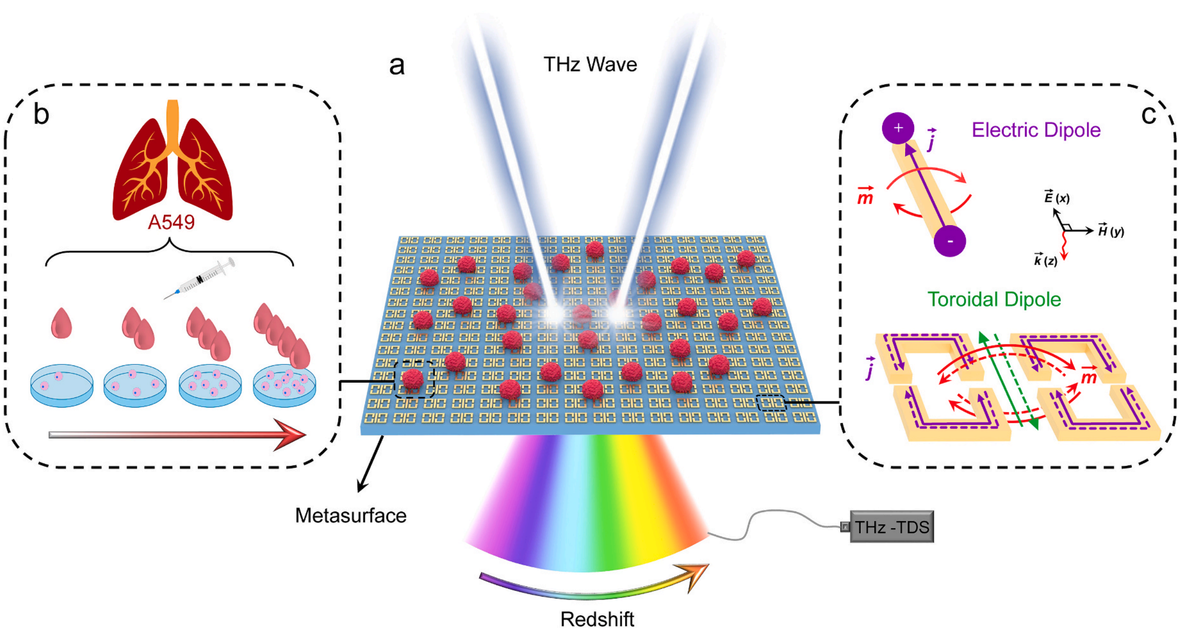

Fig. 1. The schematic of the sensing strategy based on the proposed meta-biosensor. (a) The transmission dip variations are captured by the terahertz time-domain spectroscopy (THz-TDS) when THz waves illuminating on the metasurface. (b) Lung cancer cells (type A549) with increasing concentrations are cultured on the biosensors in an environment conducive to cell reproduction. (c) The unit cell can be split into two parts including a cut wire and two mirrored SRRs for governing electric and toroidal dipole, respectively. The solid and dashed lines with arrow are used to depict the distribution of the currents and magnetic fields of the two hybridized modes as well as the toroidal dipole vector (green arrow).

(j, violet arrow) in the two loops of each dual SRRs oscillated in opposite directions, as shown in the bottom of Fig. 1(c). Both above structures can produce the similar magnetic field distribution in the near field zone and radiation patterns like doughnuts in the far field zone. Therefore, the interference between the electric and toroidal dipole occurs when illuminated by a normal incidence wave with electric fields directed along the *x*-axis. According to the right-handed screw rule, the direction of the current generated by the head-to-tail magnetic field to the direction on the cut wire is the same and opposite on mode I and mode II, respectively. This means that the electric dipole will be enhanced or weakened owing to the toroidal dipoles with different orientations.

3. Simulation and discussion

3.1. Modes analysis

In Fig. 2(a), we show the detailed geometrical parameters of meta-atom we designed. The electromagnetic response of such a hybrid resonator is numerically studied using a commercially available frequency-domain solver Computer Simulation Technology (CST) Microwave Studio. In simulated transmission spectrum as shown in Fig. 2(b), two resonance dips are clearly found at f_1 and f_2, which we labelled as mode I and mode II and highlighted by the red and blue regions, respectively. By setting field monitors at f_1 and f_2, we could attain the surface current (Fig. 2(c)(d)) and the magnetic field (Fig. 2(e)(f)) distributions. When the wave irradiates the surface of metasurface with the identical phase, we found that the surface currents on SRRs at f_1 and f_2 are distributed in the internal and external rotation, respectively, while on cut wire in the same directions. It clearly characterizes that the fields generated by the mirrored SRRs could enhance and weaken the fields generated by the cut wire on mode I and mode II, respectively. Moreover, the simulated magnetic surface currents confined in the middle of meta-atoms on mode I are remarkably higher compared to those on mode II, as shown in Fig. 2(e)(f), which also verifies that the toroidal dipole generated by two mirrored SRRs to Mode I is a promotion and a cancellation to mode II for electric dipoles generated by cut wire. The influence of the field significantly determined the power of light–matter interactions and the value of *Q* factor for sensing Gupta and Singh (2020); Keller et al. (2017).

3.2. Multipole analysis

Furthermore, we rely on the multipole expansion, Vrejoiu (2002); Gray (1978) which is based on the expansion of either potentials or fields, to help us understand this complicated interference system more clearly. A direct Taylor expansion of charge and current densities, the electric dipole, P, and the toroidal dipole, T, in Cartesian coordinate and in Gaussian units can be described as Talebi et al. (2018).

$$\mathbf{P} = \frac{1}{i\omega}\int \mathbf{j} d^3 r, \tag{1}$$

$$\mathbf{T} = \frac{1}{10c}\int \left[(\mathbf{r}\cdot\mathbf{j})\mathbf{r} - 2r^2\mathbf{j}\right] d^3 r, \tag{2}$$

where j and r are the current density and the displacement vectors, respectively. The expressions of other primary multipoles such as magnetic quadrupole, M, electric quadrupole, Q_e, and magnetic quadrupole, Q_m, could be found in Refs. Papasimakis et al. (2016); Kaelberer et al. (2010). Further, the multipole expansion of the scattered power (I_s) is calculated Kaelberer et al. (2010):

$$\begin{aligned} I_s = {} & \frac{2\omega^4}{3c^3}|\mathbf{P}|^2 + \frac{2\omega^4}{3c^3}|\mathbf{M}|^2 + \frac{4\omega^5}{3c^4}|\mathbf{P}\cdot\mathbf{T}|^2 + \frac{2\omega^6}{3c^5}|\mathbf{T}|^2 \\ & + \frac{\omega^6}{5c^5}\sum |Q_e|^2 + \frac{\omega^6}{20c^5}\sum |Q_m|^2 + O\left(\frac{1}{c^5}\right). \end{aligned} \tag{3}$$

Concretely, the scattered powers and phase of various multipole moments for the proposed structures are shown in Fig. 3, calculated from surface currents (j) via commercial simulation package Comsol Multiphysics. The detailed calculation steps can be found in the Supporting

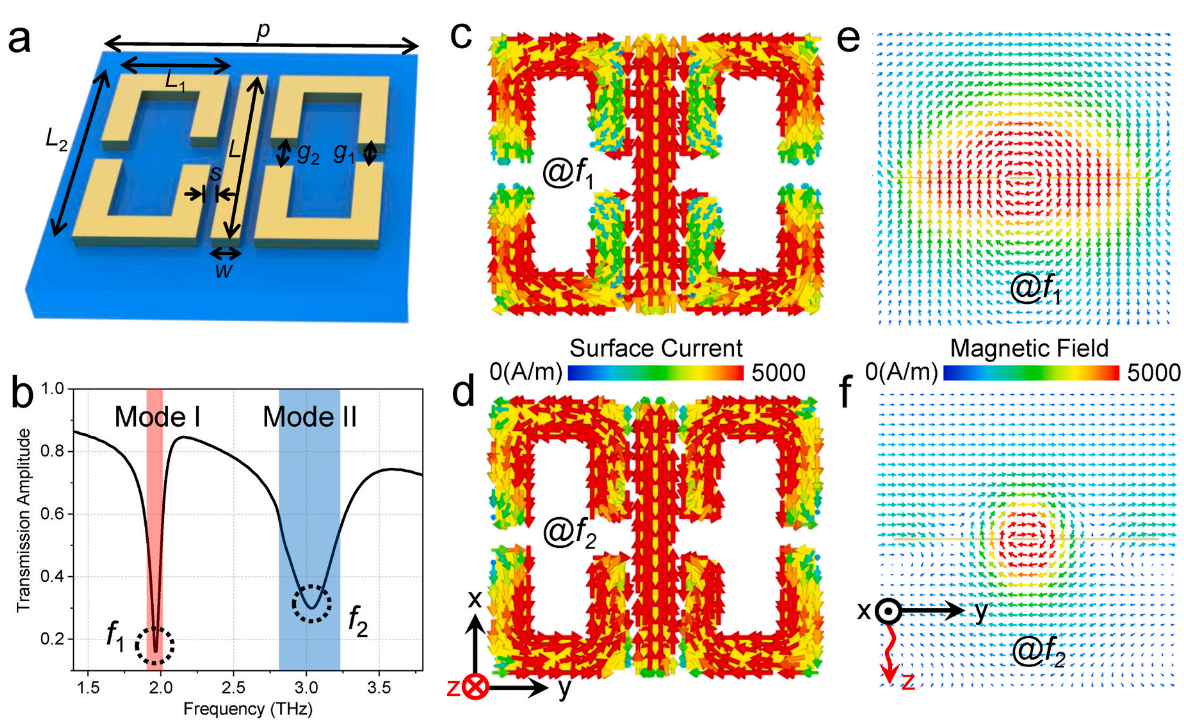

Fig. 2. The characteristic of the unit cell on different modes. (a)Unit cell of the metasurface, whose structural parameters are p = 55 μm, L_1 = 1.5 μm, L_2 = 8 μm, g_1 = 18 μm, g_2 = 2.5 μm, w = 4 μm, and L = 35 μm. (b)The transmission amplitude of the metasurface versus frequency. The resonances at f_1 and f_2 are marked as mode I (red) and mode II (blue), respectively. The surface current distributions at (c) f_1 and (d) f_2 from front view. The magnetic field distributions at (e) f_1 and (f) f_2 from side view.

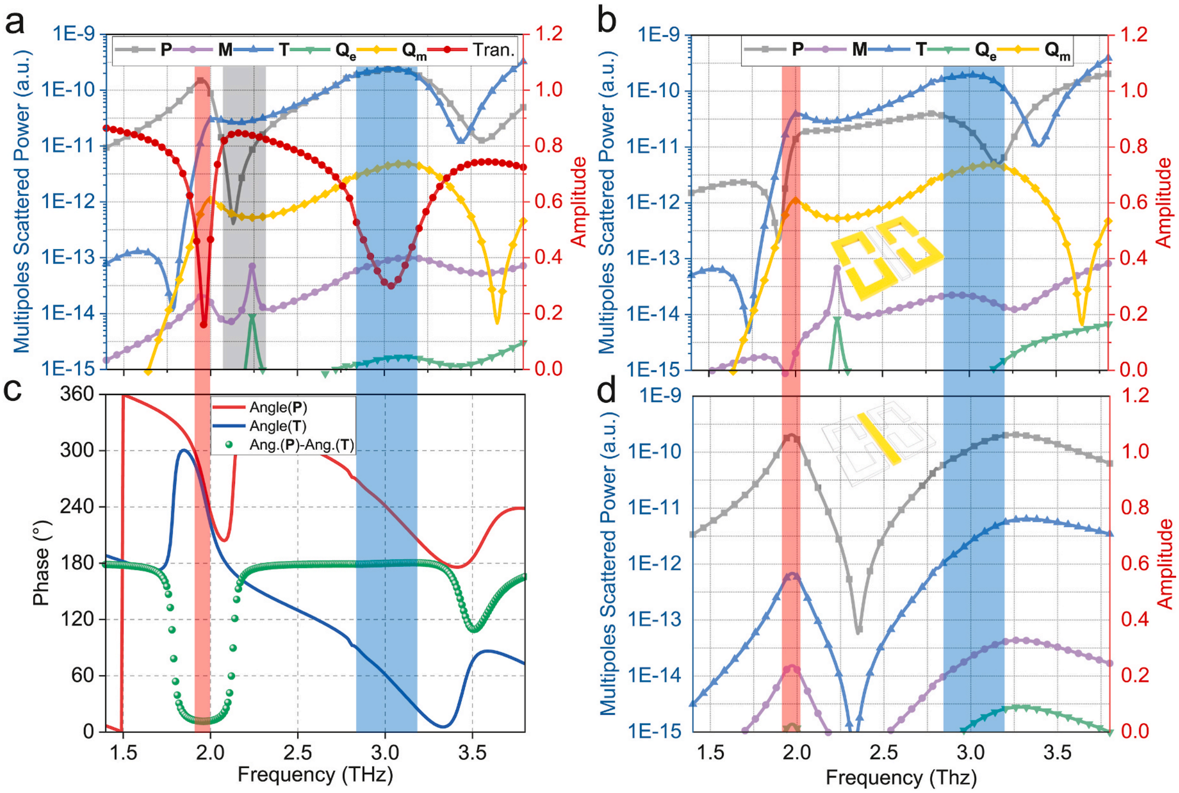

Fig. 3. The multipole scattered characteristics. Calculated scattered power for individual electromagnetic multipoles induced in metasurface by the incident radiation including electric dipole, P, magnetic dipole, M, toroidal dipole, T, electric quadrupole, Q_e, and magnetic quadrupole, Q_m. (a) The scattered power for all metallic resonant parts and the transmission amplitude. The multipoles scattered power for (b) SRRs and (d) cut wire structures in the unit cell. (c) Phase of Cartesian P and T. The green dots represent the phase difference between them.

Information S1.

We mark the red and blue regions according to the resonance dips of the transmission curve corresponding to mode I and mode II, respectively, as shown in Fig. 3(a). For mode I, the electric dipole emission is about 8.2 and 176.2 times stronger than that of the toroidal dipole and magnetic quadrupole, respectively, which clearly dominates in the window around 1.95 THz. Therefore, the sharp resonance for mode I can be called electric resonance, which is different from the general electric resonance produced by a single cut wire. The synchronous phase (~0°) also confirms that the P is enhanced by the T to exhibits a high Q factor, as illustrated in Fig. 3(c). Conversely, For mode II, the scattered power of the toroidal dipole has approached the electric dipole and the phase difference is nearly opposite (~180°). Thereby the two dipoles interfere destructively, resulting in a hybridized resonance with a low Q factor. Besides, in gray region toroidal dipole strongly suppresses the scattering of other multipoles including electric dipole as shown in Fig. 3(a), which affects the transmission amplitude and thus the resonance of the adjacent red region.

To quantitatively analyse how the two resonant structures contribute to the overall scattered power, we calculated the scattered components on for the cases of only SRRs and only cut wires, as shown in Figs. 3(b) and (d), respectively. The dual SRRs contribute most (over 99%) to the toroidal dipole moment and the magnetic quadrupole moment, and minority to the electric dipole moment for total scattering power, whiles the cut wire contributes most (over 90%) to the electric dipole moment. Therefore, we can manipulate the electric and toroidal dipole by independently changing the specific sizes of the two separated resonant structures to adjust the resonance spectrum.

3.3. Q factor optimization

Then, we optimal the Q factor and intensity of resonance spectrum by changing the length of the cut wires, L. The Q factor is commonly used to describe the narrow resonance features and can be estimated by $Q = \omega_0/\Delta\omega$, where $\Delta\omega$ is the fullwidth at half maximum (FWHM) of the resonance intensity and ω_0 is the resonance frequency. These resonance parameters are obtained by fitting a multivariate curve to the transmission amplitude, as following equation that describes the Fano resonance Talebi et al. (2018); Tan et al. (2020),

$$T(\omega) = T_0 + H\frac{(W+q)}{(1+q^2)(1+W^2)}, W = \frac{\omega - \omega_0}{\Delta\omega/2}, \tag{4}$$

where T_0 and H are constants, q is the asymmetry parameter that determines the resonance profile, while W is a normalized expression containing the resonance frequency ω_0 and $\Delta\omega$. As shown in Fig. 4(a), the Q factor of the electric resonance varies as the length of wire structure increases, changing the resonant frequency on both modes. The Q factor on mode I reaches the maximum value of 45.9 when $L = 21$ μm, after the peak Q factor decreases with growing length. It is also seen that, although the Q factor for mode II increases as for longer length L, it is still maintained at a significantly lower level. We also attain Q factor with increasing L when the single cut wire resonant, which stays low around 10. Another index, the resonance intensity defined as, $\Delta I = I_{peak} - I_{dip}$, is also significant for evaluating resonance in terms of practical applications such as sensing, since it is meaningless in the case $L = 21$ μm, where Q factor is very high but the intensity is very low, as shown in Fig. 4(b). To balance the two aspects, the resonance with $L = 35$ μm is selected, which has both a relatively high Q factor of 23.1 and a high intensity of 0.7. This trade-off is beneficial for practical sensing applications Cong et al. (2018, 2015a). It is worth emphasizing that the Q factor of resonance on mode I with same intensity is multiplied over the other plasmonic THz metasurface with similar configuration Cong et al. (2015b). Fig. 4(c) shows the transmission amplitude as functions of both

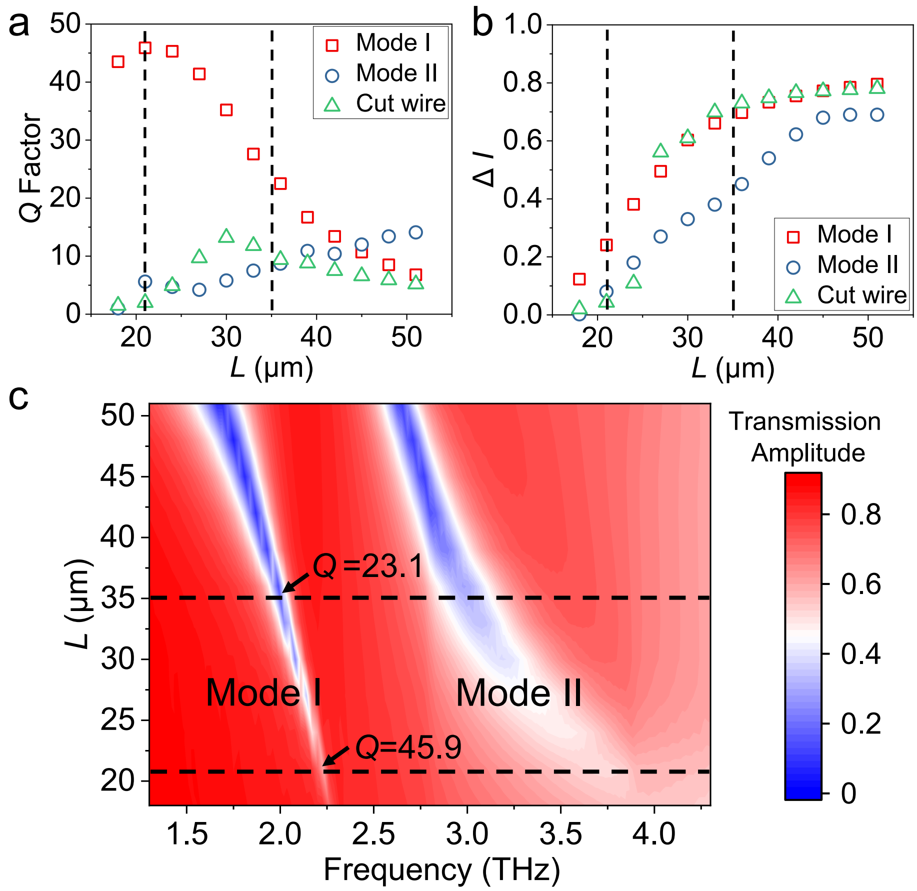

Fig. 4. Resonant metasurface properties extracted from simulations. Variation of Q factor and intensity with changing parameter Q. (a) Q factor and (b) transmission intensity change ΔI of mode I (red) and mode II (blue) resonances at different length L of the cut wire with the other parameters unchanged. (c) Transmission amplitude as a function of the parameter L and frequency of the incident THz wave.

L and frequency, which obviously shows the two dip zones corresponding to the two modes. When L increasing from 18 μm to 51 μm, the transmission amplitude of the resonance dip decreases for both modes, which implies that the resonance strength enhances. For mode I the linewidth gradually widens with L increasing, whiles for mode II it becomes narrower and varies insignificantly when exceeding 40 μm.

4. Sensing performance

Next, the sensing performance of the optimized metasurface biosensor ($L = 35$ μm) is further numerically studied. In the simulation, we assume the thickness of the analyte is 20 μm, which is comparable to the real size of a spherical A549 lung cancer cell. The assumption of equivalent randomly distributed cells into a isotropic substrate is verified by simulation, as discussed in the Supporting Information S2. We consider the analyte is non-magnetic ($\mu_r = 1$), the dielectric properties depend on the distinctive complex relative permittivity ($\epsilon_r = \epsilon_r^{'} + i\epsilon_r^{''}$) of the material itself. Then the refractive index (n) is related to real part of permittivity by equation $n = \sqrt{\mu_r \cdot \epsilon_r^{'}} = \sqrt{\epsilon_r^{'}}$. And the dielectric dissipation factor (tanδ) can also be derived from $\tan\delta = \epsilon_r^{''} / \epsilon_r^{'}$, where $\epsilon_r^{''}$ is imaginary part of permittivity. Therefore, n and tanδ could comprehensively characterize the dielectric properties of the analyte from the real and imaginary parts, respectively.

4.1. Frequency variation

For one thing, we vary the refractive index n of the analyte from 1 to 1.8 and keep its dielectric dissipation loss tanδ as 0.03 to examine the response of the transmission spectra for mode I and mode II. As illustrated in Fig. 5(a), both resonances occur almost linear redshifts as n increases. Compared to mode II, the variation of resonance dips in mode I shows a better linearity for both amplitude and frequency, as well as narrower linewidth, which are feasible for detecting and estimating matters with high accuracy and credibility. As shown in Fig. 5(b), with the change of n, the linear relationships on mode I for frequency and amplitude are fitting with the expressions $f = -0.4037 \times n + 2.36$ and $A = 0.165 \times n + 0.0464$. The slope in the curve related to frequency, i.e., the sensitivity (S_n), is as high as 403.7 GHz/RIU (Refractive Index Unit).

4.2. Amplitude variation

For another thing, the effect of the dissipation loss (tanδ) on the spectral lines is also examined numerically, as shown in Fig. 5(d). When varying the value of tanδ and keeping $n = 1.4$, it is seen that the transmission amplitudes for both modes have significant changes with negligibly weak frequency variations. With the increase of tanδ from 0 to 0.12, both two resonance dips become flatter, which leads to lower Q factors. Fig. 5(e) shows the trend of resonance dips vary with tanδ, where the amplitude follows the asymptotic exponential with the curve $A = 0.546 - 0.362 \times 0.0000438^{\tan\delta}$ by fitting. Finally, the effects of both the amplitude and frequency for these two factors (n and tanδ) are presented in the Figs. 5(c) and (f), respectively. This could help us to understand the spectral shifts as well as facilitate the prediction of the dielectric properties of tested cells.

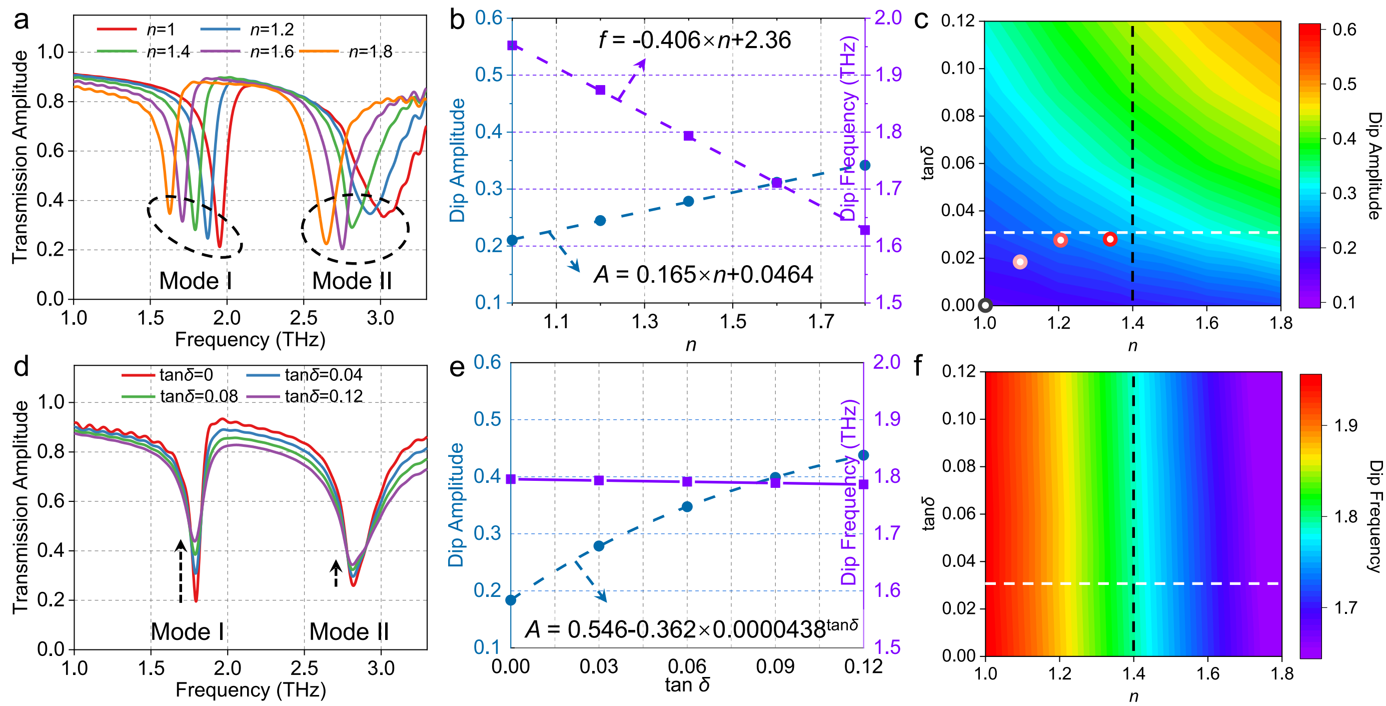

Fig. 5. The sensing characteristics of the biosensor in simulation. (a) The transmission amplitudes when refractive index n changes from 1 to 1.8 and tan δ is set to 0.03 as white dash line shown in (c). (b) The amplitude and frequency of the resonant dips on mode I are extracted for linear fitting. The variation for the (c) amplitude and (f) frequency of resonant dips both with n and tan δ. (d) The transmission amplitudes when tan δ changes from 0 to 0.12 and refractive index n is set to 1.4 as black dash line shown in (f). (e) The amplitude and frequency of the resonant dips on mode I are extracted for exponential fitting.

5. Experiment and results

5.1. Cell cultivation

We experimentally detected the lung cancer cells by the proposed biosensor. When THz waves illuminating on the metasurface biosensor cultured cells with different concentrations, the transmission spectra will occur redshift as well as amplitude variation, which could be accurately acquired by THz-TDS (ADVANTEST TAS7500SU). In our experiment, the A549 lung cancer cells are attained from the Central Laboratory of Shanghai Chest Hospital and are cultured in Roswell Park Memorial Institute (RPMI) 1640 medium (Sigma) containing 10% fetal bovine serum (Gibco), 100 IU/ml penicillin, and 100 μg/ml streptomycin (Procell) at 37°C with 5% CO_2 in a humidified atmosphere. Firstly, the adherent cells in the logarithmic growth phase are collected after a series of process including digesting with 0.25% trypsin Ethylenediaminetetraacetic acid (EDTA) solution (keyGEN) and centrifugal at 125×g for 5 min. Secondly, the cell numbers are counted in order to resuspend the cells to a certain concentration with fresh medium. For improving the utilization of cells, we design a short round acrylic tube with an inner diameter of 8 mm to place on the quartz substrate, barely reveal the biosensor in the central position. After the proposed biosensor and the acrylic tubes are sterilized and placed in 6-well plates, vaseline is smeared outside of the tube-biosensor junction to ensure the water-tightness. Finally, the preplanned cell suspension of certain concentration is seeded on the surface of the biosensor and cultured again in the environment mentioned above. It is noted that we wash the fabricated biosensor twice gently by phosphate-buffered saline (PBS) solution (Beyotime) before measurement and soak up water from the edges by blotting papers to minimize the absorption of water on THz waves. The schematic drawings of experiment details were described in Supporting Information S3. In order to avoid time-sensitive effect, all data were attained after the THz spectrum had stabilized (about 6 min), means that the surface of the sample is dry enough and the cells are still alive at this moment.

After the above preparation, we obtained the samples cultured by A549 lung cancer cells with different concentrations including 200, 500, and 800 cells/mm^2, whose micrographs are shown in Fig. 6(a–c). It is observed that different numbers of cells are covered randomly to the surface of the sensors with even distributions, so that the covered cell layer can be approximately treated as an isotropic medium. For a better view of the cells, two characteristic zones circled by the dashed line are enlarged, as shown in Figs. 6(e) and (f). The A549 cells are spherical in shape and have similar density inside and outside the metasurface region. Here, the bare biosensor, as shown in Fig. 6(d), is regarded as a reference for those samples cultured cells.

5.2. THz spectrum measurements

Fig. 7(a) shows the measured transmission spectra when the concentrations of A549 lung cancer cells on the biosensors are 200, 500, and 800 cells/mm^2. The black curve, corresponds to the bare biosensor, is a reference curve and has a very good agreement with the simulation one. Both modes occur spectral redshift when the cell concentration increase from bare to 800 cells/mm^2 but exhibit different line shapes. Fig. 7(b) shows the variation of the transmission spectra for mode II, where insignificant and irregular amplitude changes as well as flat dips are found, implying low accuracy for the detection and data processing. The maximum difference of amplitude in the regions of dashed opaque box is less than 0.005. Fortunately, the sharp dips based on the high-Q electric resonance for mode I have clear variation on both amplitude and frequency, reaching the maximum values of 146 GHz and 0.108, respectively, as shown in Fig. 7(c). The detailed experimental Q factor value for mode I and mode II could be found in Supporting Information S4. Fig. 7 (d) shows the two-dimensional fingerprint spectrum drawn by the amplitude and frequency of the resonance dips. According to the data obtained from the measurement results, we fit two dashed curves based on linear and logarithmic relationship for cell concentration in blue and red region for frequency and amplitude, where the Limit of detection (LoD) and maximum relative standard deviation (RSD) is 1.3, 45.1 cells/

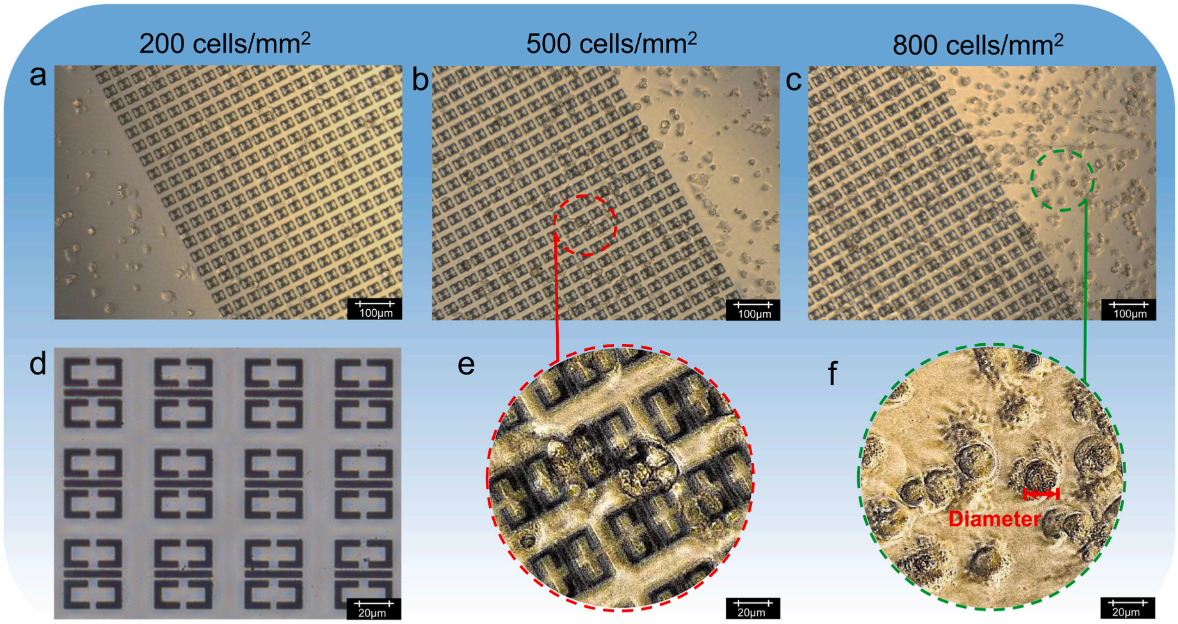

Fig. 6. The micrograph images of the fabricated meta-biosensor and the cultured lung cancer cells. Lung cancer cells at different concentrations including (a) 200 cells/mm^2, (b) 500 cells/mm^2, and (c) 800 cells/mm^2; the scale bar is 100 μm. (d) Partial view of the bare biosensor. The areas circled in (b) and (c) are shown with zoom as in (e) and (f), respectively; the scale bar is 20 μm.

mm^2, and 1.24%, 0.14% respectively. The detailed calculation can be find in Supporting Information S5. It is worth mentioning that the frequency LoD can be improved by extending the scan time of the THz-TDS system ($f_{\min} = 1/T_s$). By this, we can quickly estimate the exact cell concentration instead of traditional time-consuming counting methods.

5.3. Estimation of permittivity and cell concentration

Furthermore, the dielectric properties of the lung cancer cells could be evaluated by the previous fitting curves in simulation. Here, the tanδ variation will not shift the frequency of the resonant dip while influenced by n and the amplitude is determined by both n and tan δ, which associated with the real and imaginary parts of permittivity ϵ_r, respectively. Therefore, the frequency and amplitude of the cell could be defined as follows:

$$\begin{aligned} f_{\text{total}}^{C} &= f_0 - \Delta f_n^C, \\ A_{\text{total}}^{C} &= A_0 + \Delta A_n^C + \Delta A_{\tan\,\delta}^C \end{aligned} \tag{5}$$

where $c = 200, 500, 800$ cells/m^2 represents the concentration of cells, f_0 and A_0 are the experimental resonant frequency and amplitude of the bared biosensor, Δf_n^C and $\Delta A_{\tan\,\delta}^C$ is the difference for frequency and amplitude resulting from the change of n and tan δ, respectively. Based on the simulation and experimental results by Equation (5), the dielectric properties of the A549 cells with the concentration of 200, 500, and 800 cells/mm^2 can be evaluated approximately as shown in the Table I. More estimation of linear range and saturation range when the cell concentration is at the hypothetical maximum could be found in Supporting Information S6. Reversibly, the cell concentration can be estimated by frequency (blue) and amplitude (red) confidence intervals in Fig. 7(d), instead of relying only on a single criterion of frequency shift. The experimental sensitivity S_{exp} could be calculated by $S_{\text{exp}} = \Delta f_n^C/\Delta C = 51$ (GHz)/300 (cells/mm^2) = 0.17 GHz/(cells/mm^2). Also, the investigation of complex permittivity or refractive index with concentration provides a significant physical feature for a better knowledge of the lung cancer cells.

6. Conclusion

In this paper, we have proposed a general strategy for the design of high-Q electric dipole resonance through the interference with a toroidal dipole. We have designed a metasurface with such a hybridized resonance mode, showing a Q factor as high as 45.9, which is 5 time higher as compared to conventional single electrical resonance. We also quantified the scattered power contribution of the dominant dipoles at the working frequencies with the assistance of the multipole expansion. Further, the biosensor based on above metasurface was examined for sensing A549 lung cancer cells with different concentrations. The sensitivity of the proposed biosensor is found to be as high as 403.7 GHz/RIU. It is worth noting that the sensing performance of our proposed meta-biosensor can be enhanced in terms of sensitivity and lowweight by a microfluidic architecture as Xu et al. (2021) introduced. We show experimentally that both the resonance frequency and amplitude vary significantly when the cell concentration increases. By combining simulated and measured results, we estimated the permittivities for different concentrations of cells, which enriches the data on physical parameters of cancer cells and is expected to influence more extensive detection strategies. The proposed meta-biosensor with high Q factor electrical resonance enhanced by toroidal dipole extends the study of interference resonance and presents a promising avenue for label-free and real-time biomedical detections.

Author contribution

Chiben Zhang: Investigation, Methodology, Software, Data curation, Visualization, Writing-Original draft preparation. TingJia Xue: Investigation, Methodology, Formal analysis Validation. Jin Zhang: Methodology, Writing Reviewing and Editing. Zhenfei Li: Experiment, Writing Reviewing and Editing. Longhai Liu: Resources, Experiment, Writing Reviewing and Editing. Jianhua Xie: Resources, Project administration. Guangming Wang: Supervision, Writing Reviewing and Editing. Jianquan Yao: Supervision, Writing Reviewing and Editing, Project administration. Xiaodan Ye: Supervision, Writing Reviewing and Editing. Weiren Zhu: Conceptualization, Supervision, Writing Reviewing and Editing.

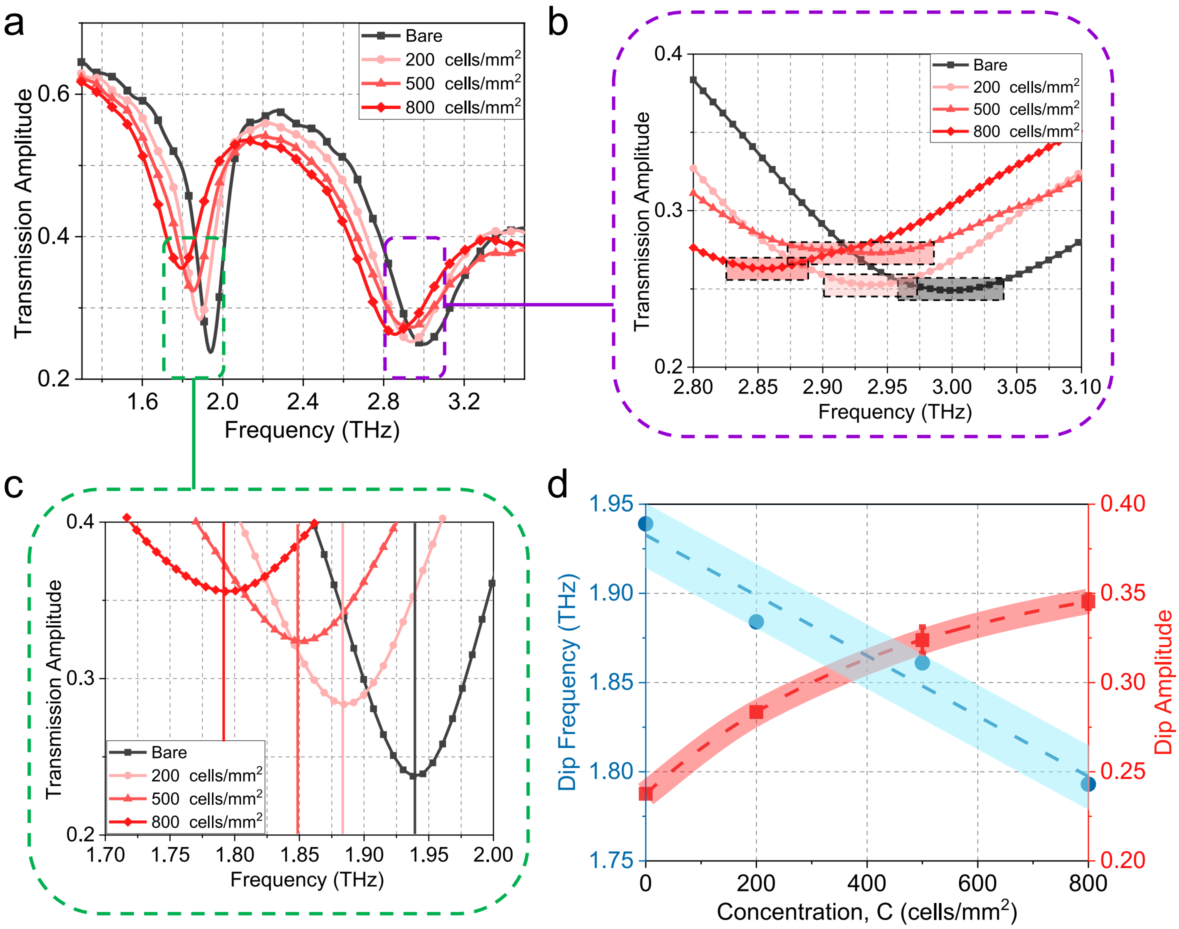

Fig. 7. The measured transmission spectra of the proposed biosensor covered by lung cancer cells with type of A549. (a) Transmission amplitude of the biosensor with different concentrations and the bare biosensor as control group. The zoom view on (b) mode II and (c) mode I in violet and green dashed box, respectively. (d) The measured frequency (blue) and amplitude (red) of resonance dip on mode I. Each sample is measured three times by THz-TDS, which shown by error bars. The fitting dashed lines for frequency and amplitude are follow linear and nonlinear variation, respectively, as predicted by the simulation. Here, the linear fitting curve for frequency follows $f = 1.93267–1.69184E\text{-}4 \times C$ and the coefficient of determination, R-Square, is 0.95935.

Table 1
The dielectric properties of A549 lung cancer cells with different concentrations.

Concentration (cells/mm^2)	Bare (0)	200	500	800
Frequency (THz)	1.939 (1.952)[a]	1.884 (1.918)	1.861 (1.867)	1.793 (1.816)
Amplitude	0.2376 (0.1562)	0.2835 (0.2021)	0.3238 (0.2424)	0.3454 (0.2640)
Refractive index (n)	Air (1)[b]	1.089	1.214	1.340
tan δ	Air (0)	0.0175	0.0270	0.0275
Permittivity ($\epsilon_r = \epsilon_r' + i\epsilon_r''$)	Air (1)	1.168 + 0.0208i	1.474 + 0.0398i	1.796 + 0.0494i

[a] The numbers in bracket are the results after normalization to bare sample and fitting according to linear variation.
[b] Here, we assume that the permittivity of air is ideal as 1.

Declaration of competing interest

The authors declare that they have no known competing financial interests or personal relationships that could have appeared to influence the work reported in this paper.

Acknowledgements

This work was supported by National Natural Science Foundation of China (NSFC) (82071990, 81571629, 62071291, 61871394), Project of Shanghai Science and Technology Commission (19411965200) and Shanghai Chest Hospital Project of Collaborative Innovative Grant YJT20191015.

Appendix A. Supplementary data

Supplementary data to this article can be found online at https://doi.org/10.1016/j.bios.2022.114493.

References

Alici, K.B., 2014. Hybridization of fano and vibrational resonances in surface-enhanced infrared absorption spectroscopy of streptavidin monolayers on metamaterial substrates. IEEE Trans. Nanotechnol. 13 (2), 216–221.
Cheng, R., Xu, L., Yu, X., Zou, L., Shen, Y., Deng, X., 2020. High-sensitivity biosensor for identification of protein based on terahertz fano resonance metasurfaces. Opt Commun. 473, 125850.
Cong, L., Manjappa, M., Xu, N., Al-Naib, I., Zhang, W., Singh, R., 2015a. Fano resonances in terahertz metasurfaces: a figure of merit optimization. Adv. Opt. Mater. 3 (11), 1537–1543.
Cong, L., Savinov, V., Srivastava, Y.K., Han, S., Singh, R., 2018. A metamaterial analog of the ising model. Adv. Mater. 30 (40), 1804210.
Cong, L., Tan, S., Yahiaoui, R., Yan, F., Zhang, W., Singh, R., 2015b. Experimental demonstration of ultrasensitive sensing with terahertz metamaterial absorbers: a comparison with the metasurfaces. Appl. Phys. Lett. 106 (3), 031107.
Dubovik, V., Tugushev, V., 1990. Toroid moments in electrodynamics and solid-state physics. Phys. Rep. 187 (4), 145–202.
Flambaum, V., Murray, D., 1997. Anapole moment and nucleon weak interactions. Phys. Rev. C 56 (3), 1641.
Flambaum, V.V., Khriplovich, I.B., 1980. P-odd nuclear forces: a source of parity violation in atoms. J. Exp. Theor. Phys. 52 (5), 5.

González-Alcalde, A.K., Mandujano, M.A.G., Salas-Montiel, R., Le Cunff, L.O., Lerondel, G., Méndez, E.R., 2019. Magnetic mirror metasurface based on the in-phase excitation of magnetic dipole and electric quadrupole resonances. J. Appl. Phys. 125 (24), 243103.

Gray, C., 1978. Multipole expansions of electromagnetic fields using debye potentials. Am. J. Phys. 46 (2), 169–179.

Guo, L.Y., Li, M.H., Huang, X.J., Yang, H.L., 2014. Electric toroidal metamaterial for resonant transparency and circular cross-polarization conversion. Appl. Phys. Lett. 105 (3), 033507.

Gupta, M., Singh, R., 2020. Terahertz sensing with optimized Q/v_{eff} metasurface cavities. Adv. Opt. Mater. 8 (16), 1902025.

Huang, Y.W., Chen, W.T., Wu, P.C., Fedotov, V.A., Zheludev, N.I., Tsai, D.P., 2013. Toroidal lasing spaser. Sci. Rep. 3 (1), 1–4.

Kaelberer, T., Fedotov, V., Papasimakis, N., Tsai, D., Zheludev, N., 2010. Toroidal dipolar response in a metamaterial. Science 330 (6010), 1510–1512.

Keller, J., Scalari, G., Cibella, S., Maissen, C., Appugliese, F., Giovine, E., Leoni, R., Beck, M., Faist, J., 2017. Few-electron ultrastrong light-matter coupling at 300 ghz with nanogap hybrid lc microcavities. Nano Lett. 17 (12), 7410–7415.

Kerker, M., Wang, D.S., Giles, C.L., 1983. Electromagnetic scattering by magnetic spheres. J. Opt. Soc. Am. 73 (6), 765–767.

Lemak, S., Beloglazova, N., Nocek, B., Skarina, T., Flick, R., Brown, G., Popovic, A., Joachimiak, A., Savchenko, A., Yakunin, A.F., 2013. Toroidal structure and dna cleavage by the crispr-associated [4fe-4s] cluster containing cas4 nuclease sso0001 from sulfolobus solfataricus. J. Am. Chem. Soc. 135 (46), 17476–17487.

Li, Z., Zhang, D., Liu, J., Zhang, J., Shao, L., Wang, X., Jin, R., Zhu, W., 2022. 3-d manipulation of dual-helical electromagnetic wavefronts with a noninterleaved metasurface. IEEE Trans. Antenn. Propag. 70 (1), 378–388.

Li, Z.F., Qiao, P.W., Dong, G.Y., Shi, Y.S., Bi, K., Yang, X.L., Meng, X.F., 2018. Polarization-multiplexed broadband hologram on all-dielectric metasurface. Europhys. Lett. 124 (1), 14003.

Liu, W., Kivshar, Y.S., 2018. Generalized kerker effects in nanophotonics and meta-optics. Opt Express 26 (10), 13085–13105.

Lou, J., Yang, R., Liang, J., Yu, Y., Zhang, L., Zhang, C., Li, T., Fan, Y., Zhang, F., Wang, G., et al., 2021. Dual-sensitivity terahertz metasensor based on lattice–toroidal-coupled resonance. Adv. Photon. Res. 2 (4), 2000175.

Naumov, I.I., Bellaiche, L.M., Prosandeev, S.A., Ponomareva, I.V., Kornev, I.A., 2009. Ferroelectric Nanostructure Having Switchable Multi-Stable Vortex States. US Patent.

Papasimakis, N., Fedotov, V., Savinov, V., Raybould, T., Zheludev, N., 2016. Electromagnetic toroidal excitations in matter and free space. Nat. Mater. 15 (3), 263–271.

Shamkhi, H.K., Baryshnikova, K.V., Sayanskiy, A., Terekhov, P.D., Gurvitz, E.A., Valero, A.C., Karabchevsky, A., Kapitanova, P., Evlyukhin, A.B., Belov, P., Kivshar, Y., Shalin, A.S., 2019. Non-huygens invisible metasurfaces. In: 2019 PhotonIcs Electromagnetics Research Symposium. Spring (PIERS-Spring), pp. 2999–3002.

Talebi, N., Guo, S., van Aken, P.A., 2018. Theory and applications of toroidal moments in electrodynamics: their emergence, characteristics, and technological relevance. Nanophotonics 7 (1), 93–110.

Tan, T.C., Plum, E., Singh, R., 2020. Lattice-enhanced fano resonances from bound states in the continuum metasurfaces. Adv. Opt. Mater. 8 (6), 1901572.

Tassin, P., Zhang, L., Koschny, T., Economou, E., Soukoulis, C.M., 2009. Low-loss metamaterials based on classical electromagnetically induced transparency. Phys. Rev. Lett. 102 (5), 053901.

Vrejoiu, C., 2002. Electromagnetic multipoles in cartesian coordinates. J. Phys. Math. Gen. 35 (46), 9911.

Wang, W., Zheng, L., Wang, Y., 2020. Polarization-independent fano metasurface with directional toroidal dipole for magnetic field tunability. Opt Commun. 454, 124516.

Wu, P.C., Liao, C.Y., Savinov, V., Chung, T.L., Chen, W.T., Huang, Y.W., Wu, P.R., Chen, Y.H., Liu, A.Q., Zheludev, N.I., et al., 2018. Optical anapole metamaterial. ACS Nano 12 (2), 1920–1927.

Xu, J., Liao, D., Gupta, M., Zhu, Y., Zhuang, S., Singh, R., Chen, L., 2021. Terahertz microfluidic sensing with dual-torus toroidal metasurfaces. Adv. Opt. Mater. 9 (15), 2100024.

Yan, X., Li, T., Ma, G., Gao, J., Wang, T., Yao, H., Yang, M., Liang, L., Li, J., Li, J., et al., 2022. Ultra-sensitive dirac-point-based biosensing on terahertz metasurfaces comprising patterned graphene and perovskites. Photon. Res. 10 (2), 280–288.

Yan, X., Yang, M., Zhang, Z., Liang, L., Wei, D., Wang, M., Zhang, M., Wang, T., Liu, L., Xie, J., et al., 2019. The terahertz electromagnetically induced transparency-like metamaterials for sensitive biosensors in the detection of cancer cells. Biosens. Bioelectron. 126, 485–492.

Yang, M., Liang, L., Zhang, Z., Xin, Y., Wei, D., Song, X., Zhang, H., Lu, Y., Wang, M., Zhang, M., Wang, T., Yao, J., 2019. Electromagnetically induced transparency-like metamaterials for detection of lung cancer cells. Opt Express 27 (14), 19520–19529.

Yang, R., Xu, J., Shen, N.H., Zhang, F., Fu, Q., Li, J., Li, H., Fan, Y., 2021. Subwavelength optical localization with toroidal excitations in plasmonic and mie metamaterials. InfoMat 3 (5), 577–597.

Yang, Y., Kravchenko, I.I., Briggs, D.P., Valentine, J., 2014. All-dielectric metasurface analogue of electromagnetically induced transparency. Nat. Commun. 5 (1), 1–7.

Yin, X., Feng, T., Yip, S., Liang, Z., Hui, A., Ho, J.C., Li, J., 2013. Tailoring electromagnetically induced transparency for terahertz metamaterials: from diatomic to triatomic structural molecules. Appl. Phys. Lett. 103 (2), 021115.

Zel'Dovich, I.B., 1958. Electromagnetic interaction with parity violation. Sov. Phys. - JETP 6 (6), 1184–1186.

Zhang, C., Wang, G., Xu, H.X., Zhang, X., Li, H.P., 2020. Helicity-dependent multifunctional metasurfaces for full-space wave control. Adv. Opt. Mater. 8 (8), 1901719.

Zhang, C., Xue, T., Zhang, J., Liu, L., Xie, J., Wang, G., Yao, J., Zhu, W., Ye, X., 2022. Terahertz toroidal metasurface biosensor for sensitive distinction of lung cancer cells. Nanophotonics 11 (1), 101–109.

Zhang, C., Zhang, X., Xie, P., Hou, H., Liu, K., Lou, J., Bai, H., Zhang, J., Li, Z., Zhu, W., Wang, G., 2021a. Filter-assisted metasurface for full-space wavefront manipulation and energy allocation. ACS Appl. Electron. Mater. 3 (10), 4465–4471.

Zhang, J., Mu, N., Liu, L., Xie, J., Feng, H., Yao, J., Chen, T., Zhu, W., 2021b. Highly sensitive detection of malignant glioma cells using metamaterial-inspired thz biosensor based on electromagnetically induced transparency. Biosens. Bioelectron. 185, 113241.

Zhang, L., Tassin, P., Koschny, T., Kurter, C., Anlage, S.M., Soukoulis, C.M., 2010. Large group delay in a microwave metamaterial analog of electromagnetically induced transparency. Appl. Phys. Lett. 97 (24), 241904.